Optical Fiber Refractive Index Profiling by Iterative Optical Diffraction Tomography

Shengli Fan , Seth Smith-Dryden, Jian Zhao , Stefan Gausmann, Axel Schülzgen , *Fellow, OSA*,
Guifang Li, *Fellow, IEEE, Fellow, OSA*, and Bahaa E. A. Saleh , *Life Fellow, IEEE, Fellow, OSA*

***Abstract*—A non-destructive iterative interferometric tomographic technique is proposed for imaging fibers with high refractive index contrast, complex structures, and/or large optical path differences. Both simulation and experimental results demonstrate that this technique enables the reconstruction of fiber refractive index profiles accurately and robustly with sub-wavelength resolution.**

***Index Terms*—Iterative reconstruction algorithms, optical diffraction tomography, optical fiber measurements.**

I. INTRODUCTION

QUANTITATIVE refractive-index profiling is highly desired in the design and manufacturing of optical fibers and fiber devices [1]–[4]. While topographic techniques require cleaving at the plane of measurement and careful etching and calibration [5], optical tomographic methods are non-destructive and do not require sample cleaving. If diffraction effects are negligible, as in the short-wavelength case, imaging of optical fibers can be assumed to follow a ray-optics model and reconstruction methods based on computed tomography (CT) [6], [7], such as optical phase tomography [8], [9], can readily be used. However, when the wavelength of illumination is on a scale similar to the sample feature size, the wave nature of light must be accounted for. Optical diffraction tomography (ODT) [10] was developed for this purpose. So far, ODT has been used for imaging a large-mode-area photonic-crystal fiber in the visible and near-infrared regimes [11] and also for applications in label-free biological imaging [12] with sub-wavelength resolution [13].

In ODT, the object to be imaged is transversely illuminated at each angle, and the diffracted field is measured. Under the weak-scattering condition, the diffracted fields are linearly related to the refractive index (RI) distribution of the object, through the use of the first-Born [14] or Rytov [15] approximation. Unfortunately, these linear inversion algorithms fail when the weak-scattering condition is not satisfied, as is the case for samples with high RI contrast, complex structures, and/or large optical path differences (OPDs) against the background, which cause multiple scattering [16]–[18]. In these scenarios, the inversion problem becomes very challenging.

In this paper, an iterative optical diffraction tomography (iODT) algorithm is proposed and tested for the reconstruction of optical fiber RI profiles beyond the weak-scattering regime. This iterative algorithm seeks to improve reconstruction quality by iteratively minimizing the error between the field diffracted by the reconstructed object and the field measured experimentally or obtained through simulations of phantoms. Based on the error calculated from a previous estimate of the RI profile, a perturbative correction to the RI profile is computed, forming a new estimate for the next iteration. Both simulation and experimental results demonstrate that the proposed iODT algorithm can provide robust and accurate reconstruction of optical fiber profiles with high RI contrast, complex structures, and/or large OPDs.

II. RECONSTRUCTION ALGORITHM

A reconstruction algorithm aims at the inversion of a forward model relating the diffracted field to the object RI distribution. Reasonable assumptions are usually adopted to render the inversion feasible and efficient. In this section, we first discuss the standard ODT inversion that is based on the Born or Rytov approximation, which linearizes the relation between the diffracted field and the object function. We then introduce the framework of iODT, which is based on iterative perturbation for which the relation between the perturbative diffracted fields and the perturbative object function is linearized in each iteration, though ultimately the reconstructed object is nonlinearly related to measured diffracted fields.

The tomographic imaging configuration is shown in Fig. 1. For simplicity, two-dimensional (2D) phase objects are considered in this paper, but extending the analysis to three-dimensional objects is straightforward. The phase object to be reconstructed (e.g., an optical fiber cross-section) has a RI profile $n(x,y) = n_b + \Delta n(x,y)$, where n_b is the RI of the background. The contrast of the object is defined by the ratio $\max|\Delta n(x,y)|/n_b$. The object is illuminated by a set of plane waves with propagation constant k_b directed at different angles and the diffracted field is measured at each angle to form a sinogram. For illumination at an angle θ, the incident and diffracted fields $u_0(\xi,\eta)$ and $u(\xi,\eta,\theta)$ are expressed in the
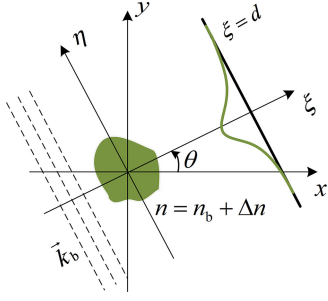
Fig. 1.   Schematic of the tomographic imaging configuration.

rotated "local" coordinates (ξ, η) which are related to the fixed "global" coordinates (x, y) by the relations: $x = \xi\cos\theta - \eta\sin\theta$ and $y = \xi\sin\theta + \eta\cos\theta$. Both ODT and iODT rely on Fourier transform operations. Throughout this paper, we use the same symbol to designate a function and its Fourier transform; for example, $\psi(k_\eta, \theta)$ is the one-dimensional (1D) Fourier transform of $\psi(\eta, \theta)$ with respect to η.

A. Optical Diffraction Tomography

Conventional computed tomography (CT) is applicable to low-contrast phase objects with feature sizes much greater than the wavelength of the probe light so that diffraction is negligible. With a ray-optics forward model, measurement at each angle produces a projection of the object function, which can be used to obtain a slice of the Fourier transform of the object function in accordance with the projection-slice theorem. The measurements constitute a Radon transform, which may be inverted by means of filtered backprojection (FBPJ) [19].

When the feature size of a low-contrast phase object is comparable with the wavelength, the effects of diffraction cannot be ignored. Under the condition of weak scattering, the Born or Rytov approximation is used to linearly relate the measured fields to the object function $f(x, y) = (2\pi k_0)^2 [n^2(x, y) - n_{\rm b}^2]$. ODT reconstruction relies on the diffraction-slice theorem [20] whose inversion is commonly performed by filtered backpropagation (FBPP) [21]. In this paper, we will adopt the Rytov approximation, which has been shown to be typically superior to the Born approximation [22].

When reconstructing an off-axis object, the defocused optical field may fluctuate rapidly and the validity of the Rytov approximation then breaks down. A modified FBPP algorithm, called the extended-depth-of-focus (EDOF) FBPP, offers considerable improvements in the reconstruction of features at locations offset from the center of rotation [23]. The Rytov-based EDOF-FBPP algorithm involves the following steps:

i) The measured field is backpropagated through the background medium to obtain the field $u(\xi, \eta, \theta)$ from which the Rytov complex phase is computed

$$\varphi_{\rm R}(\xi, \eta, \theta) = \ln\frac{u(\xi, \eta, \theta)}{u_0(\xi, \eta)}. \qquad (1)$$

ii) The complex phase is unwrapped and filtered in the spectral domain,

$$\Pi_{\rm EDOF}(\xi, k_\eta, \theta) = \varphi_{\rm R}(\xi, k_\eta, \theta) |k_\eta| . \qquad (2)$$
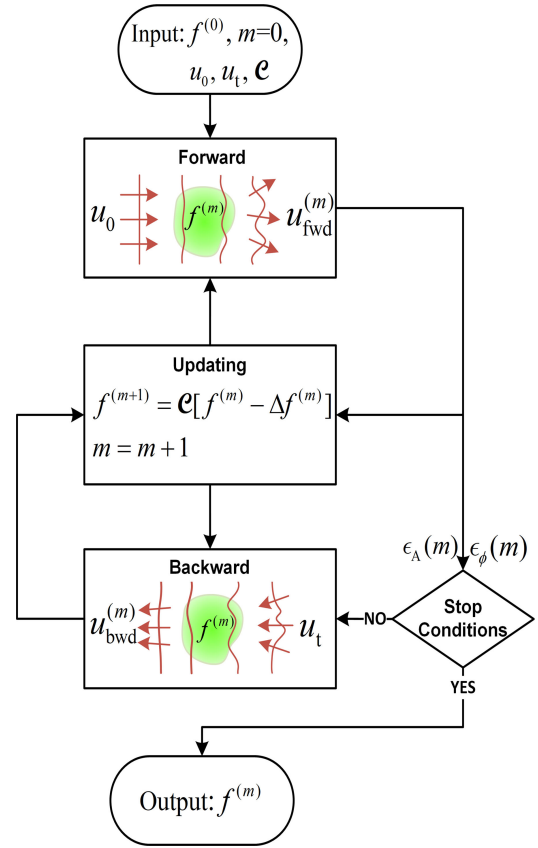

Fig. 2.   Block diagram of the iODT algorithm. $f^{(0)}$: an initial guess of the object function; m: the iteration number; $f^{(m)}$: the reconstructed object function in the $m^{\rm th}$ iteration; u_0 : the known incident wave (plane wave); $u_{\rm t}$: the true field, which is obtained experimentally or through simulations of phantoms; $\mathcal{C}$: a constraint operator; $u_{\rm fwd}^{(m)}$: the 2D forward-propagated incident field through the reconstructed object $f^{(m)}$; $u_{\rm bwd}^{(m)}$: the 2D backward propagated true field through the reconstructed object $f^{(m)}$; $\epsilon_{\rm A}(m), \epsilon_\phi(m)$: the normalized root-mean-square errors in the amplitude and phase of the sinograms in the $m^{\rm th}$ iteration, respectively.

iii) The inverse Fourier transform of $\Pi_{\rm EDOF}(\xi, k_\eta, \theta)$ is summed over all illumination angles to reconstruct the object function

$$f(x, y) = -j2\pi k_{\rm b} \int_0^{2\pi} \Pi_{\rm EDOF}(\xi, \eta, \theta) d\theta. \qquad (3)$$

B. Iterative Optical Diffraction Tomography

For phase objects having high RI contrast, complex structures, and/or large OPDs against the background, multiple scattering occurs and introduces nonlinearities between the measured field and the object function, which will render the linear reconstruction methods (including CT and ODT) ineffective. To reduce the reconstruction errors caused by multiple scattering, we propose an iODT algorithm, schematically shown in Fig. 2. This method aims at improving the reconstruction quality by iteratively reducing the error between the fields that are diffracted by the reconstructed object, and the true fields that are measured experimentally or obtained through simulations of phantoms, for all illumination angles. The true field $u_{\rm t}(\xi = d, \eta, \theta)$ is obtained by measuring the complex field in the plane of the CCD

camera and backpropagating it to the $\xi = d$ plane through free space and any intervening optical elements (This may also be accomplished by forward propagating the field from the plane conjugate to the camera plane to the $\xi = d$ plane through background medium).

The iterative algorithm is based on successive improvements on estimates of the object function. If in the mth iteration $f^{(m)}(x, y)$ is a known imperfect estimate of the true object function $f(x, y)$, and if the field generated by forward propagating the known incident field $u_0(\xi, \eta)$ through $f^{(m)}(x, y)$ at angle θ is $u_{\text{fwd}}^{(m)}(\xi, \eta, \theta)$, then the associated complex phase is $\varphi_{\text{R}}^{(m)}(\xi, \eta, \theta) = \ln \frac{u_{\text{fwd}}^{(m)}(\xi, \eta, \theta)}{u_0(\xi, \eta)}$. The perturbative complex phase is then

$$\Delta\varphi_{\text{R}}^{(m)}(\xi, \eta, \theta) = \ln \frac{u_{\text{fwd}}^{(m)}(\xi, \eta, \theta)}{u_0(\xi, \eta)} - \ln \frac{u_{\text{t}}(\xi, \eta, \theta)}{u_0(\xi, \eta)}$$
$$= \ln \frac{u_{\text{fwd}}^{(m)}(\xi, \eta, \theta)}{u_{\text{t}}(\xi, \eta, \theta)}, \qquad (4)$$

where $u_{\text{t}}(\xi, \eta, \theta)$ is the true, but unknown, field throughout the scattering area/volume. In conventional ODT, $u_{\text{t}}(\xi, \eta, \theta)$ is estimated by backpropagating the true field $u_{\text{t}}(\xi = d, \eta, \theta)$ through the background medium, but since we now have a known estimate $f^{(m)}(x, y)$ of the object, we heuristically use instead the measured field backpropagated through the estimated object, which we denote $u_{\text{bwd}}^{(m)}(\xi, \eta, \theta)$. It follows that

$$\Delta\varphi_{\text{R}}^{(m)}(\xi, \eta, \theta) \approx \ln \frac{u_{\text{fwd}}^{(m)}(\xi, \eta, \theta)}{u_{\text{bwd}}^{(m)}(\xi, \eta, \theta)}. \qquad (5)$$

If the estimated object $f^{(m)}(x, y)$ equals the true object $f(x, y)$, then $u_{\text{fwd}}^{(m)}(\xi, \eta, \theta) = u_{\text{bwd}}^{(m)}(\xi, \eta, \theta)$ for all angles, and the perturbation $\Delta\varphi_{\text{R}}^{(m)}(\xi, \eta, \theta) = 0$. This is the perfect solution consistent with both input and output boundary conditions. Since this condition is not generally satisfied, we use this perturbation $\Delta\varphi_{\text{R}}^{(m)}(\xi, \eta, \theta)$ to calculate the corresponding correction to the reconstructed object function, $\Delta f^{(m)}(x, y) = f^{(m)}(x, y) - f(x, y)$, by means of formulae derived from Eqs. (2) and (3):

$$\Delta\Pi_{\text{EDOF}}^{(m)}(\xi, k_\eta, \theta) = \Delta\varphi_{\text{R}}^{(m)}(\xi, k_\eta, \theta)|k_\eta|, \qquad (6)$$

$$\Delta f^{(m)}(x, y) = -j2\pi k_{\text{b}} \int_0^{2\pi} \Delta\Pi_{\text{EDOF}}^{(m)}(\xi, \eta, \theta) d\theta. \qquad (7)$$

We now use the correction $\Delta f^{(m)}(x, y)$ to determine a new estimate for the true object function, $f^{(m+1)}(x, y) = f^{(m)}(x, y) - \Delta f^{(m)}(x, y)$, where $m = 0, 1, \ldots$ is the iteration number as illustrated in the block diagram in Fig. 2. If the initial guess $f^{(0)}(x, y) = 0$, then the first iteration of the iODT generates a reconstructed object function $f^{(1)}(x, y)$ identical to that of conventional ODT. Prior information on the true object function $f(x, y)$ may be used to apply constraints, such as non-negativity or reality, on the estimated object function $f^{(m)}(x, y)$ at each iteration. The algorithm is then described by the iterative relation

$$f^{(m+1)}(x, y) = \mathcal{C}[f^{(m)}(x, y) - \Delta f^{(m)}(x, y)], \qquad (8)$$

where $\mathcal{C}$ is a constraint operator. To implement the iODT algorithm, it is necessary to solve the forward and backward propagation problems at each angle for each iteration. An accurate and efficient forward solver $\boldsymbol{S}$ is used to calculate the forward-propagated field $u_{\text{fwd}}^{(m)}(\xi, \eta, \theta) = \boldsymbol{S}[u_0, f^{(m)}(x, y), \theta]$, which is generated by the incident wave u_0 as it propagates through the object $f^{(m)}(x, y)$ at each angle θ. The same solver is used in the reverse direction to calculate the backward propagated field $u_{\text{bwd}}^{(m)}(\xi, \eta, \theta) = \boldsymbol{S}^{-1}[u_{\text{t}}(d, \eta, \theta), f^{(m)}(x, y), \theta]$, which results from backpropagating the true field $u_{\text{t}}(d, \eta, \theta)$ through the estimated object at each angle θ.

The proposed iODT algorithm also needs a proper convergence criterion. Furthermore, it is desirable to institute a stopping criterion independent of the object. When the error between the estimated sinogram $u_{\text{fwd}}^{(m)}(d, \eta, \theta)$ and the true sinogram $u_{\text{t}}(d, \eta, \theta)$ converges, the correction to the object function will be negligible in comparison with the object function itself. To characterize the deviation between the estimated sinogram and the true sinogram in each iteration, we define the normalized-root-mean-square (nRMS) error between these two sinograms in both amplitude and phase

$$\epsilon_{\text{A}}(m) = \frac{\sqrt{\sum \left[|u_{\text{t}}(\eta, \theta)| - |u_{\text{fwd}}^{(m)}(\eta, \theta)|\right]^2 / N_{\text{pix}}}}{\text{range}\left[|u_{\text{t}}(\eta, \theta)|\right]}, \qquad (9)$$

$$\epsilon_{\phi}(m) = \frac{\sqrt{\sum \left\{\boldsymbol{W}\left[\text{Arg}\, u_{\text{t}}(\eta, \theta) - \text{Arg}\, u_{\text{fwd}}^{(m)}(\eta, \theta)\right]\right\}^2 / N_{\text{pix}}}}{\text{range}\left\{\boldsymbol{W}[\text{Arg}\, u_{\text{t}}(\eta, \theta)]\right\}}, \qquad (10)$$

where N_{pix} is the number of pixels in the sinogram, $\boldsymbol{W}$ is a phase-wrapping operator, $\text{Arg}\{\cdot\}$ returns the principal value of phase, and the argument $\xi = d$ is ignored for brevity. When convergence is achieved, the variation of the nRMS errors ϵ_{A} and ϵ_{ϕ} will be vanishingly small for successive Q iterations. If these errors fail to converge before a predefined maximum number of iterations, the iterative reconstruction will be terminated at this predefined number. Therefore, we select the stop conditions as follows

$$\begin{aligned} &|\epsilon_{\text{A}}(m) - \epsilon_{\text{A}}(m-q)| < \epsilon_{\text{tol}}, \\ &|\epsilon_{\phi}(m) - \epsilon_{\phi}(m-q)| < \epsilon_{\text{tol}}, \\ &\text{or } m > m_{\max}, \end{aligned} \qquad (11)$$

where ϵ_{tol} is predefined tolerance level, parameter $q = 1, 2, \ldots Q$, and $m_{\max}$ is the predefined maximum number of iterations.

III. RECONSTRUCTION RESULTS

We have verified the effectiveness of the iODT algorithm for objects with high RI contrast, complex structures, and/or large OPDs by both simulations and experiments. In simulation verifications, the true sinograms are obtained from phantoms using the finite-difference time-domain (FDTD) method [24], which is considered the most accurate. In experimental verifications, the interferograms are measured using a Mach-Zehnder interferometer (see Fig. 11) and the true sinograms are extracted from the interferograms. In the iterative reconstruction process,

an accurate and efficient numerical solver is highly desirable in order to calculate the forward and backward fields in Eq. (5) for all illumination angles. In this paper, we use the wide-angle beam propagation method (WABPM) [25], instead of FDTD which is also the most time-consuming, as the numerical solver for each iteration. The L2-norm method [26] is used to unwrap the complex phase. To suppress high-frequency noise, the ramp filter in Eq. (6) can be replaced by a Shepp-Logan-Gaussian filter, which is a product of a Shepp-Logan filter [20] and a Gaussian filter. For constraints, non-positivity or non-negativity will be applied to the real part of reconstructed RI distribution if it is a priori known that the background medium has, respectively, largest or smallest RI. Since we are more interested in phase objects, a non-imaginary constraint will also be applied to the reconstructed object function. For the stop condition, the sinogram errors are compared for the successive $Q = 10$ iterations and the error tolerance level ϵ_{tol} is chosen to be 10^{-3}. The iODT algorithm is implemented in MATLAB 2016a and the simulation is conducted in a computer equipped with an Intel(R) Core(TM) i7-5820K 3.3 GHz CPU and a 32GB RAM.

A. Validation Based on Simulated Data

True sinograms from phantoms with high contrast, complex structures, and/or large OPDs, consisting of diffracted fields corresponding to illumination angles from 0° to 355° with an increment of 5°, are calculated using the FDTD method. If the phantom or the reconstructed object in each iteration has rotational symmetry of order α, only the fields corresponding to the angles from 0° to 360°/α need to be calculated. The wavelength of the probe light λ_0 is 650 nm and the RI of the background medium n_b is 1.4584 so that the wavelength in this medium λ_b is 445.7 nm For the following examples, we will use these wavelengths and background RI, unless otherwise specified.

1) Two-Core Fiber

In this example, the phantom is a two-core fiber with core diameters of 20 μm separated by 30 μm, and a core-cladding/background RI contrast of 10%. This phantom is used to validate the effectiveness of iODT in reconstructing objects with high RI contrast and large OPD ($11.1\lambda_b$ in this case). The computational domain is sampled with grid size $\Delta x = \Delta y = \lambda_b/2$. The data processing time of iODT reconstruction is approximately 0.4 minutes per iteration. The RI distribution of the phantom and the reconstructed object using three different algorithms, CT, ODT and iODT ($m = 21$), are shown in Fig. 3, and their horizontal cross sections are plotted in Fig. 4. In the CT reconstruction, there are many artifacts between the two cores as well as around the background because the phase unwrapping, applied on the sinogram, undergoes significant failures which contaminate the reconstruction. In the ODT reconstruction, EDOF-FBPP propagates the field in the background medium, thus can model the defocused field to some extent. The modelling of the defocused field is more accurate for illumination angles at which the two cores are approximately aligned in the transverse direction so that the probe beam is
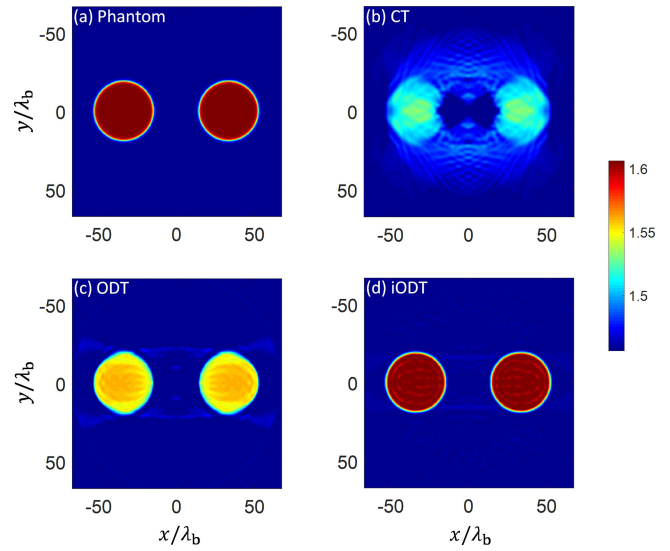

Fig. 3. (a) RI distribution of the phantom of a two-core fiber (10% contrast). Reconstructions using (b) CT, (c) ODT, and (d) iODT ($m = 21$).
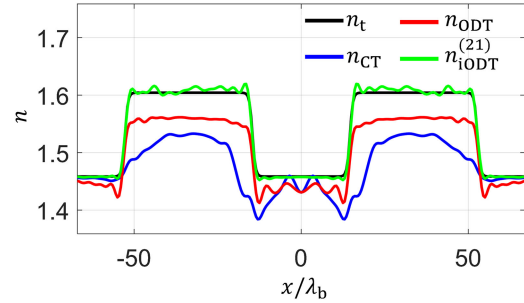

Fig. 4. 1D cross sections of the phantom and reconstructions using CT, ODT and iODT ($m = 21$).

diffracted by each core independently. The phase unwrapping, applied locally on the back-propagated fields, performs well for these angles. Therefore, the artifact in the reconstructed RI distribution in the transverse direction is suppressed. However, for the remaining illumination angles where the two cores are aligned approximately along the wave propagation direction, the defocused field cannot be accurately modelled by EDOF-FBPP because of multiple scattering. As a result, the phase differences against the background are still large and have phase vortices, causing phase-unwrapping failures, which introduce errors into the reconstructed RI. To consider the multiple-scattering effect in the iODT reconstruction, plane waves and true fields are forward and backward propagated, respectively, for each illumination angle, through an estimate of RI distribution instead of the background medium. The perturbative complex phase remains small and therefore can be successfully unwrapped. The RI distribution reconstructed by iODT (see Fig. 3) is the more accurate in terms of shape, RI values and artifact suppression, as quantified below.

The nRMS errors in the amplitude and phase of the sinograms as functions of the iteration number are shown in Fig. 5(a) and (b), respectively. Since the 2π phase ambiguities are gradually removed by phase unwrapping in each iteration, the nRMS
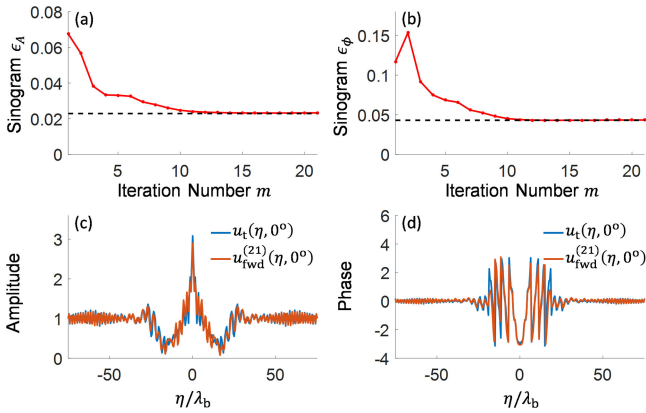
Fig. 5. The nRMS errors in the amplitude (a) and the phase (b) of the sinograms as functions of the iteration number m. The dashed lines in (a) and (b) indicate the floors corresponding to the discrepancy between WABPM and FDTD. The amplitude (c) and phase (d) of the field diffracted by the phantom (blue) and by the reconstructed object (red) after 21 iterations for the illumination angle of 0°.
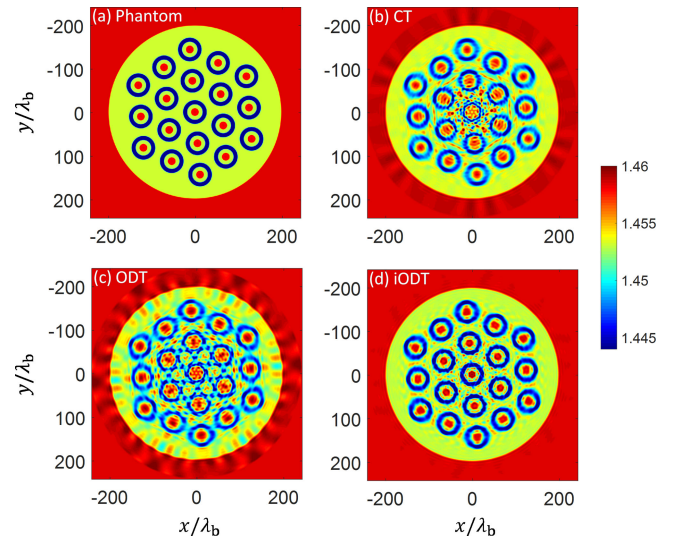

Fig. 6. (a) RI distribution of a 19-core fiber phantom. Reconstructions using (b) CT, (c) ODT, and (d) iODT ($m = 34$).
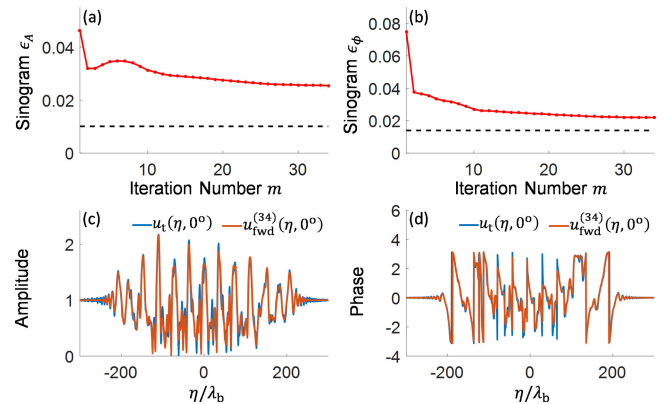

Fig. 7. The nRMS errors in the amplitude (a) and the phase (b) of the sinograms as functions of the iteration number m. The dashed lines in (a) and (b) indicate the floors corresponding to the discrepancy between WABPM and FDTD. The amplitude (c) and phase (d) of the field diffracted by the phantom (blue) and by the reconstructed object (red) after 34 iterations for the illumination angle of 0°.

error in the phase of sinograms, which is defined by the wrapped phase difference [see Eq. (10)], may diverge temporarily, after which the iteration converges quickly. The iterative reconstruction converges by 21 iterations, at which the sinogram errors approach the floors corresponding to the discrepancy between WABPM and FDTD (indicated by the dashed lines), which indicates that the object can be accurately reconstructed using the iODT method. After 21 iterations, the amplitude and phase of the field diffracted by the phantom and by the reconstructed object for the illumination angle of 0° are displayed in Fig. 5(c) and (d), respectively.

In order to assess upper limits on the contrast of objects that may be successfully reconstructed using iODT, we have tested the two-core fiber phantoms at various contrast levels (higher than the 10% example shown above). We find that the maximum RI contrast that iODT can adequately reconstruct is about 12% ($\Delta n = 0.1750$). If the contrast is 14%, then the value of the reconstructed RI is about 0.023 smaller than that of the phantom. However, the fields diffracted by the phantom and the reconstructed object match well, indicating that iODT reconstruction is trapped in a local minimum.

2) 19-Core Fiber

In this test, we create a phantom with a complex structure and large OPD ($2.5\lambda_b$) to demonstrate the effectiveness of iODT against multiple scattering. The phantom is a 19-core fiber with a cladding RI of 1.453 and cladding diameter of 180 μm. Each core has a RI of 1.458 and diameter of 9.2 μm surrounded by a trench with a width of 4.6 μm and RI of 1.444. The core-to-core distance is 32 μm. The largest RI variation $\Delta n = 0.014$ is between the trench and the core, so that the RI contrast is about 0.96%. The grid size used in the reconstruction is $\Delta x = \Delta y = \lambda_b/2$. The data processing time of iODT reconstruction is about 1.6 minutes per iteration. The RI distributions of the phantom and the reconstructed object using the CT, ODT and iODT ($m = 34$), are shown in Fig. 6. In the CT reconstruction, the phase-unwrapping failures, attributed to the

presence of phase vortices, introduce severe artifacts around the central region of the reconstruction. EDOF-FBPP, propagating the true field through the background medium, however, fails to model the defocused fields correctly because the multiple-scattering effect caused by this multi-core fiber is not negligible for all illumination angles. Ironically, the phase differences against the background field remain large and contain complex distributions, caused by phase vortices, which exacerbate the phase-unwrapping failures. Consequently, the ODT reconstruction contains more artifacts. Compared with CT and ODT, the reconstruction using iODT is more accurate in terms of RI distribution and artifact suppression.

The nRMS errors in the amplitude and phase of the sinograms as functions of the iteration number are shown in Fig. 7(a) and (b), respectively. The sinogram errors converge by 34 iterations, reducing the nRMS error in amplitude from 4.7% to 2.5% and the error in phase from 7.3% to 2.2%, respectively. The
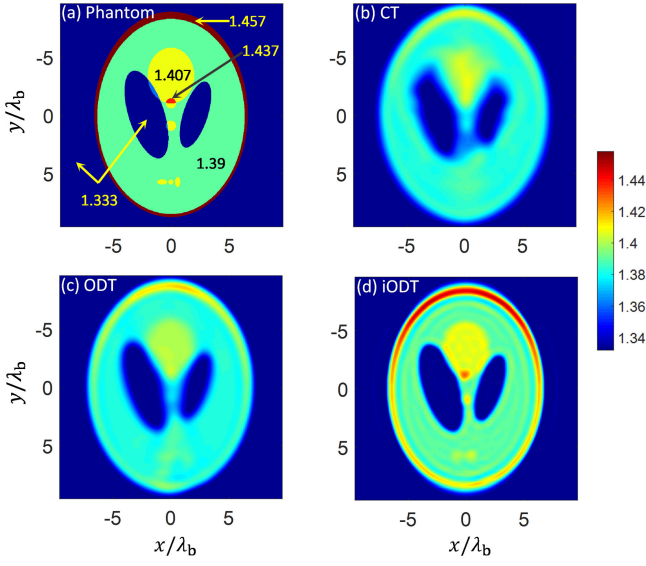
Fig. 8. (a) RI distribution of the Shepp-Logan phantom. Reconstructions using (b) CT, (c) ODT, and (d) iODT ($m = 14$).
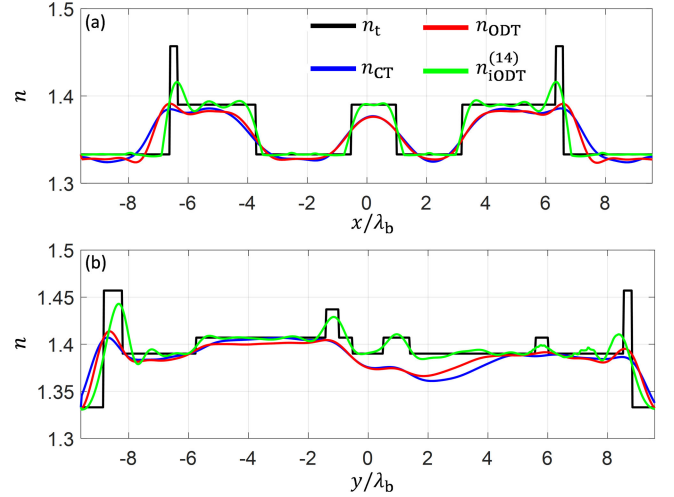

Fig. 9. Horizontal (a) and vertical (b) cross sections of the phantom and reconstructions using CT, ODT and iODT ($m = 14$).
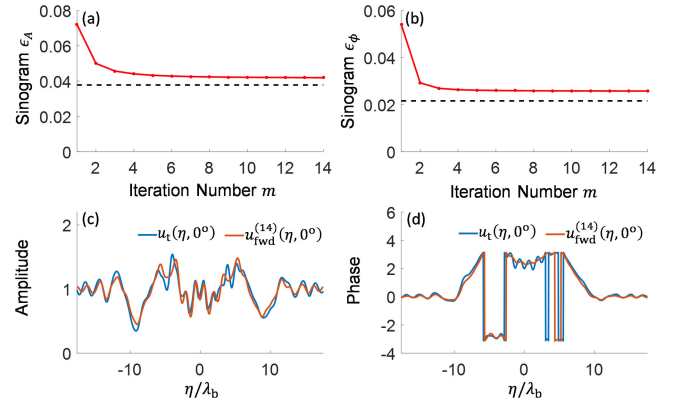

Fig. 10. The nRMS errors in the amplitude (a) and the phase (b) of the sinograms as functions of the iteration number m. The dashed lines in (a) and (b) indicate the floors corresponding to the discrepancy between WABPM and FDTD. The amplitude (c) and phase (d) of the field diffracted by the phantom (blue) and by the reconstructed object (red) after 14 iterations for the illumination angle of 0°.

nRMS errors do not reach the floors corresponding to the discrepancy between WABPM and FDTD (indicated by the dashed lines). After 34 iterations, the amplitude and phase of the field diffracted by the phantom and by the reconstructed object for the illumination angle of 0°, are shown in Fig. 7(c) and (d), respectively. We believe the reason why the nRMS errors do not reach the WABPM-FDTD floors is not due to the iODT method itself. We have verified that by increasing the angular resolution of the sinogram from 5° to 1°, the nRMS errors do reach the WABPM-FDTD floors. This is reasonable because the reduced periodicity between cores, from 180° in the previous case of the two-core fiber to 60° for the current 19-core fiber, necessitates a finer angular step size.

3) Shepp-Logan Phantom

In this example, the capability of iODT will be further demonstrated by reconstructing the well-known Shepp-Logan phantom whose parameters are labeled in Fig. 8(a) [17]. The wavelength used in this test is 406 nm and the background RI is 1.333, so that the wavelength in the background medium λ_b is 304.6 nm. The largest RI variation $\Delta n = 0.124$ is between the phantom edge and the background, therefore the RI contrast is about 9.3%. To accurately represent the small features of this phantom, a small grid size $\Delta x = \Delta y = \lambda_b/35$ is used. The data processing time of iODT reconstruction is about 3 minutes per iteration. The RI distributions of the phantom and the reconstructed object using the CT, ODT and iODT ($m = 14$), are shown in Fig. 8, and their horizontal and vertical cross sections are displayed in Fig. 9(a) and (b), respectively.

Because this phantom has feature sizes smaller than or comparable to the wavelength in the background medium and a RI contrast as high as 9.3%, the multiple-scattering effect cannot be neglected. As a result, small features in this phantom can only be resolved by iODT. In this reconstruction, a Shepp-Logan filter is employed to balance spatial resolution and artifact suppres-

sion. The three features at the bottom of the phantom are only visible in the iODT reconstruction. Since ODT and iODT have resolution of $\lambda_b/\sqrt{2}$ in the transmission configuration, the three features at the bottom of the phantom, which are smaller than $\lambda_b/2$, cannot be completely resolved, even with iODT.

The nRMS errors of the sinograms are presented in Fig. 10(a) and (b). The error in the amplitude of the sinogram decreases from 7.2% to 4.2% and the error in the phase decreases from 5.4% to 2.5%. Sinogram errors converge by 14 iterations and approximately approach the floors corresponding to the discrepancy between WABPM and FDTD (indicated by the dashed lines). The amplitude and phase of the field diffracted by the phantom and the reconstructed object for the illumination angle of 0° are shown in Fig. 10(c) and (d), respectively.

B. Experimental Validation

To evaluate the proposed iODT algorithm using experimental data, a commercial optical fiber profiler IFA-100 [27] is used
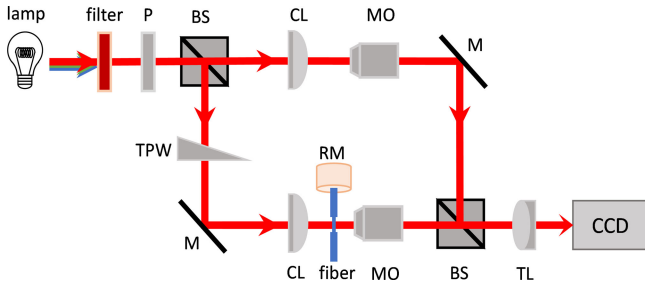
Fig. 11.　Schematic setup of the commercial profiler IFA-100. P: polarizer; BS: beam splitter; M: mirror; TPW: translating phase wedge; CL: condenser lens; RM: rotation motor; MO: microscope objective; TL: tube lens.

to collect the data. As displayed in Fig. 11, the setup is based on off-axis Mach-Zehnder phase-shifting interferometry in an object-rotating configuration. Light coming from an incandescent lamp, passing through a narrow-band filter and polarizer, is split into a reference beam and an object beam, both of which are rendered to be plane waves after the condensers. The sample to be imaged is held transversely to the illumination and controlled by a rotation motor. The interference between the object and reference arms are captured through an imaging system consisting of high-NA, oil-immersion objectives (25×, NA = 1.4) and a tube lens by a CCD camera to create a digital hologram. The complex fields are extracted from the measured interferograms by the Fourier transform method [28] or the Hilbert transform method [29]. The true fields u_t are obtained by forward propagating the field from the plane conjugate to the camera plane to the $\xi = d$ plane through the background medium. The data acquisition time is about one minute for each illumination angle.

1) 19-Core Single-Mode Fiber

In this experiment, we choose a 19-core single-mode fiber, modeled earlier by the phantom in Section III-A, designed for spatial-division multiplexing [30], [31] as a test sample. The central wavelength of the narrow-band filter used in the experiment is 650 nm, at which the RI of the matching oil is 1.4584. Since the sample to be imaged, unlike the phantom shown in the previous examples, does not have rotational symmetry, interferograms corresponding to illumination angles extending from 0° to 355°, with an increment of 5°, are recorded using the profiler.

The grid size in the reconstruction is $\Delta x = \Delta y = 4.6/25 = 0.184$ μm, which equals the pixel size of the CCD camera divided by the magnification of the objective. The data processing time of iODT reconstruction is 10.2 minutes per iteration. The true sample, unlike the phantom of 19-core fiber shown in the previous case, does not have rotational symmetry of order 6, so that the reconstruction processing time is approximately scaled by a factor of 6. The microscopic image of the sample and the reconstructed RI distributions, using CT, ODT and iODT ($m = 13$) algorithms are shown in Fig. 12. In the CT reconstruction, the inability of modelling the defocused field accentuates the phase-unwrapping failures, resulting in large errors in the middle of the reconstruction. ODT, even when combined with extended depth of focus, also fails to model the defocused field correctly for all illumination angles, due to the fields only being backpropagated through the background medium. The
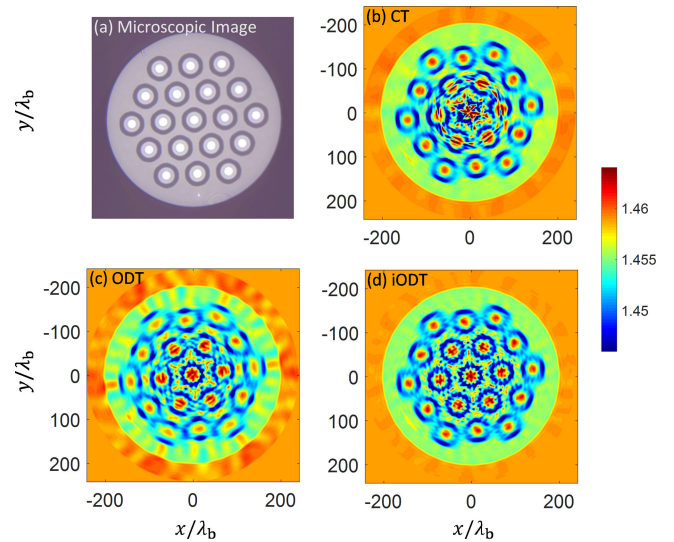

Fig. 12.　(a) Microscopic image of the 19-core single-mode fiber. Reconstructions using (b) CT, (c) ODT, and (d) iODT ($m = 13$).
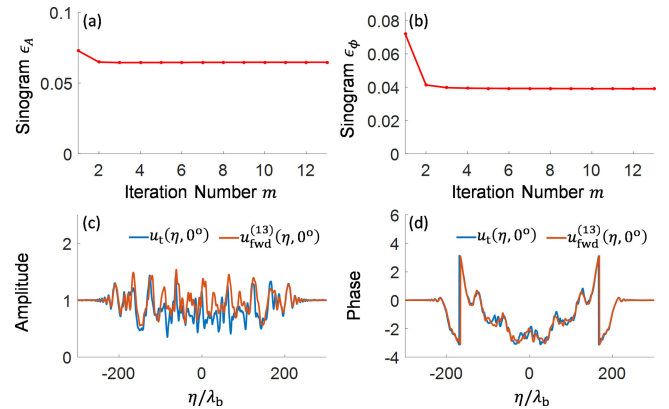

Fig. 13.　The nRMS errors in the amplitude (a) and the phase (b) of the sinograms as functions of the iteration number m. The amplitude (c) and phase (d) of the experimental field (blue) and the simulated field diffracted by the reconstructed object (red) after 13 iterations for the illumination angle of 0°.

phase differences against the background are not only large but complicated in their distributions, due to phase vortices. Therefore, more drastic failures in phase unwrapping are introduced, which results in reconstruction artifacts. The smearing effect in the iODT reconstruction may be related to the uncertainty of the rotation angles in the experiment, due to the fiber not rotating as a rigid object, with respect to the rotational mount.

The dependence of the nRMS errors in the amplitude and phase of the sinograms versus the iteration number are presented in Fig. 13(a) and (b), respectively. The sinogram errors decrease from 7.0% to 6.0% in the amplitude, and from 7.5% to 3.9% in the phase. Sinogram errors converge by 13 iterations. The amplitude and phase of the experimental field and the simulated field, which is diffracted by the reconstructed object, for the illumination angle of 0° are shown in Fig. 13(c) and (d), respectively.

2) Leakage Channel Fiber

To further verify the effectiveness of iODT for the RI profiling of optical fibers, we provide another example of reconstructing
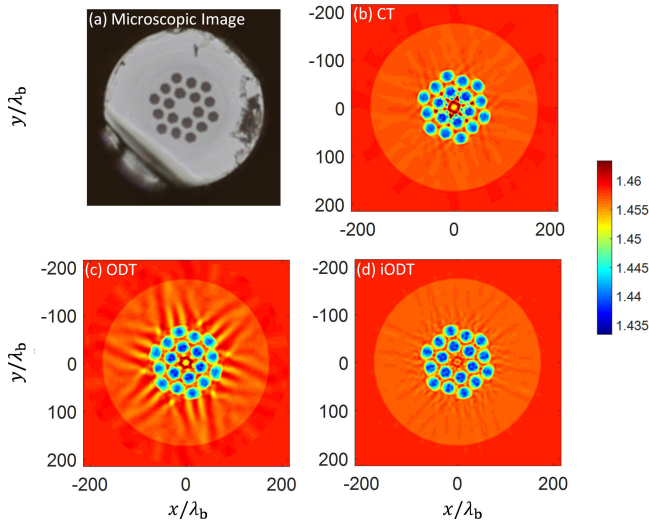
Fig. 14. (a) Microscopic image of the leakage channel fiber. Reconstructions using (b) CT, (c) ODT, and (d) iODT ($m = 12$).
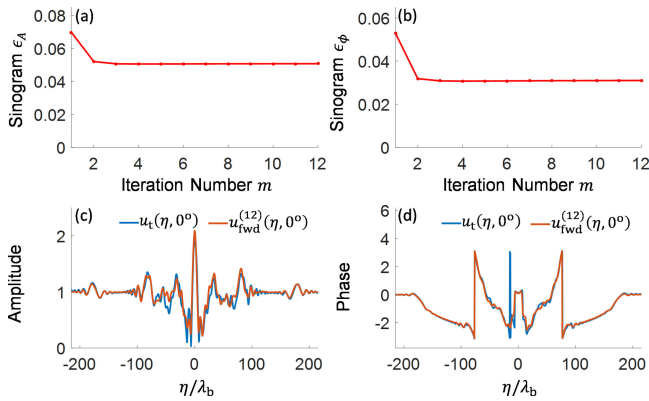

Fig. 15. The nRMS errors in the amplitude (a) and the phase (b) of the sinograms as functions of the iteration number m. The amplitude (c) and phase (d) of the experimental field (blue) and the simulated field diffracted by the reconstructed object (red) after 12 iterations for the illumination angle of 0°.

the resonantly enhanced leakage channel fiber [32], [33], whose cladding is tapered down to 160 μm. The two rings of fluorine-doped silica rods have lower refractive indices than that of the cladding silica. The middle core is also made of silica. The grid size used in the reconstruction is $\Delta x = \Delta y = 4.6/25 = 0.184$ μm. The data processing time of iODT reconstruction is about 8 minutes per iteration. The microscopic image of this fiber and the reconstructed RI profiles using CT, ODT and iODT ($m = 12$) are demonstrated in Fig. 14. The artifacts, shown in the central and cladding region in the CT and ODT reconstructions, respectively, are suppressed in the iODT reconstruction.

The nRMS errors of the sinograms are presented in Fig. 15(a) and (b). The sinogram error decreases from 7.0% to 5.1% in the amplitude, and from 5.3% to 3.1% in the phase. Sinogram errors converge by 12 iterations. The experimental field and the simulated field, which is diffracted by the reconstructed object, for the illumination angle of 0° are shown in Fig. 15(c) and (d).

IV. CONCLUSIONS & DISCUSSIONS

Conventional optical diffraction tomography (ODT) relies on the Rytov approximation, which is a first-order perturbation/linearization method valid for weak-scattering objects satisfying certain smoothness conditions on the refractive index distribution and limits on the optical path differences. When these conditions are not met, the approximation no longer holds and the reconstruction fails. The inversion problem is also compounded by the emergence of many phase vortices in the fields diffracted by these objects. In this paper, we have developed an iterative optical diffraction tomography (iODT) algorithm and demonstrated that it is applicable in such cases.

The first iteration of iODT provides an estimate of the unknown RI profile using the standard linearized ODT inversion algorithm. Subsequent iterations improve on this estimate by applying a perturbative correction based on differences between the fields diffracted by the imperfectly reconstructed object and the measured fields diffracted by the true object. This error is translated into an error in the associated complex phase, from which a correction to the reconstructed object function is computed. The Rytov approximation is used in every iteration as it is more applicable to the perturbative function, as opposed to the original function. Since the magnitude (distribution) of the perturbative function becomes smaller (smoother) at higher iterations, the Rytov approximation improves. Further, as expected, the number of phase vortices in the perturbative complex phase is gradually reduced in a self-healing process as the iterations converge. In essence, our iterative algorithm is a nonlinear reconstruction based on perturbative expansion, much like a higher-order Born or Rytov expansion for forward propagation.

Through numerical simulations and experimental tests applied to various optical fiber RI profiles, we have verified that this heuristic iterative algorithm provides both better accuracy and fast convergence, as well as sub-wavelength resolution. One added benefit is that the method tends to suppress errors resulting from phase-unwrapping failures, which typically occur in such field-based inverse problems. We therefore maintain that iODT offers a reliable alternative to conventional ODT for reconstructing fiber RI profiles of higher contrast, complex structures, and/or large optical path differences. For objects with contrast exceeding 12% and/or complex configurations, iODT is prone to failure primarily caused by the proliferation of phase vortices of the perturbative complex phase and phase-unwrapping errors, which result in the creation of artifacts in the reconstruction, trapping in a local minimum, or even divergence of the iterative process.

REFERENCES

[1] K. Dossou, S. LaRochelle, and M. Fontaine, "Numerical analysis of the contribution of the transverse asymmetry in the photo-induced index change profile to the birefringence of optical fiber," *J. Lightw. Technol.*, vol. 20, no. 8, pp. 1463–1470, Aug. 2002.

[2] E. Anemogiannis, E. N. Glytsis, and T. K. Gaylord, "Transmission characteristics of long-period fiber gratings having arbitrary azimuthal/radial refractive index variations," *J. Lightw. Technol.*, vol. 21, no. 1, pp. 218–227, Jan. 2003.

[3] B. L. Bachim and T. K. Gaylord, "Polarization-dependent loss and birefringence in long-period fiber gratings," *Appl. Opt.*, vol. 42, no. 34, pp. 6816–6823, Dec. 2003.

[4] H. Liu *et al.*, "Reducing group delay spread using uniform long-period gratings," *Sci. Rep.*, vol. 8, no. 1, p. 3882, Mar. 2018.

[5] S. T. Huntington, P. Mulvaney, A. Roberts, K. A. Nugent, and M. Bazylenko, "Atomic force microscopy for the determination of refractive index profiles of optical fibers and waveguides: A quantitative study," *J. Appl. Phys.*, vol. 82, no. 6, pp. 2730–2734, Sep. 1997.

[6] W. A. Kalender, "X-ray computed tomography," *Phys. Med. Biol.*, vol. 51, no. 13, pp. 29–43, Jun. 2006.

[7] J. Hsieh, *Computed Tomography: Principles, Design, Artifacts, and Recent Advances*, vol. PM259, 3rd ed. Bellingham, WA, USA: SPIE, 2015.

[8] W. Choi *et al.*, "Tomographic phase microscopy," *Nature Methods*, vol. 4, no. 9, pp. 717–719, Sep. 2007.

[9] B. L. Bachim, T. K. Gaylord, and S. C. Mettler, "Refractive-index profiling of azimuthally asymmetric optical fibers by microinterferometric optical phase tomography," *Opt. Lett.*, vol. 30, no. 10, pp. 1126–1128, May 2005.

[10] E. Wolf, "Three-dimensional structure determination of semi-transparent objects from holographic data," *Opt. Commun.*, vol. 1, no. 4, pp. 153–156, Sep. 1969.

[11] W. Gorski and W. Osten, "Tomographic imaging of photonic crystal fibers," *Opt. Lett.*, vol. 32, no. 14, pp. 1977–1979, Jul. 2007.

[12] Y. Sung, W. Choi, C. Fang-Yen, K. Badizadegan, R. R. Dasari, and M. S. Feld, "Optical diffraction tomography for high resolution live cell imaging," *Opt. Express*, vol. 17, no. 1, pp. 266–277, Jan. 2009.

[13] K. Kim, J. Yoon, S. Shin, S. Lee, S.-A. Yang, and Y. Park, "Optical diffraction tomography techniques for the study of cell pathophysiolog," *J. Biomed. Photon. Eng.*, vol. 2, no. 2, p. 020201, Jun. 2016.

[14] M. Born and E. Wolf, *Principles of Optics*, 7th ed. Cambridge, U.K.: Cambridge Univ. Press, 1999.

[15] A. J. Devaney, "Inverse-scattering theory within the Rytov approximation," *Opt. Lett.*, vol. 6, no. 8, pp. 374–376, Aug. 1981.

[16] X. Ma, W. Xiao, and F. Pan, "Optical tomographic reconstruction based on multi-slice wave propagation method," *Opt. Express*, vol. 25, no. 19, pp. 22595–22607, Sep. 2017.

[17] E. Soubies, T.-A. Pham, and M. Unser, "Efficient inversion of multiple-scattering model for optical diffraction tomography," *Opt. Express*, vol. 25, no. 18, pp. 21786–21800, Sep. 2017.

[18] T.-A. Pham *et al.*, "Versatile reconstruction framework for diffraction tomography with intensity measurements and multiple scattering," *Opt. Express*, vol. 26, no. 3, pp. 2749–2763, Feb. 2018.

[19] A. C. Kak and M. Slaney, *Principles of Computerized Tomographic Imaging*. Philadelphia, PA, USA: SIAM, 2001.

[20] B. E. A. Saleh and M. C. Teich, *Fundamentals of Photonics*, 2nd ed. New York, NY, USA: Wiley, 2007.

[21] A. J. Devaney, "A filtered backpropagation algorithm for diffraction tomography," *Ultrason. Imag.*, vol. 4, no. 4, pp. 336–350, Oct. 1982

[22] B. Chen and J. J. Stamnes, "Validity of diffraction tomography based on the first Born and the first Rytov approximations," *Appl. Opt.*, vol. 37, no. 14, pp. 2996–3006, May 1998.

[23] J. Kostencka and T. Kozacki, "Computational and experimental study on accuracy of off-axis reconstructions in optical diffraction tomography," *Opt. Eng.*, vol. 54, no. 2, p. 024107, 2015.

[24] A. Taflove and S. C. Hagness, *Computational Electrodynamics: The Finite-Difference Time-Domain Method*, 3rd ed. Boston, MA, USA: Artech House, 2005.

[25] K. Kawano and T. Kitoh, *Introduction to Optical Waveguide Analysis, Solving Maxwell's Equations and the Schrodinger Equation*. New York, NY, USA: Wiley, 2001.

[26] D. C. Ghiglia and M. D. Pritt, *Two-Dimensional Phase Unwrapping: Theory, Algorithms, and Software*. New York, NY, USA: Wiley, 1998.

[27] A. D. Yablon, "Multi-wavelength optical fiber refractive index profiling by spatially resolved fourier transform spectroscopy," *J. Lightw. Technol.*, vol. 28, no. 4, pp. 360–364, Feb. 2010.

[28] M. Takeda, H. Ina, and S. Kobayashi, "Fourier-transform method of fringe-pattern analysis for computer-based topography and interferometry," *J. Opt. Soc. Amer.*, vol. 72, no. 1, pp. 156–160, Jan. 1982.

[29] T. Ikeda, G. Popescu, R. R. Dasari, and M. S. Feld, "Hilbert phase microscopy for investigating fast dynamics in transparent systems," *Opt. Lett.*, vol. 30, no. 10, pp. 1165–1167, May 2005.

[30] G. Li, N. Bai, N. Zhao, and C. Xia, "Space-division multiplexing: The next frontier in optical communication," *Adv. Opt. Photon.*, vol. 6, no. 4, pp. 413–487, Dec. 2014.

[31] K. Takenaga *et al.*, "Reduction of crosstalk by trench-assisted multi-core fiber," in *Proc. Opt. Fiber Commun. Conf. Expo. Nat. Fiber Opt. Eng. Conf.*, 2011, pp. 1–3.

[32] R. A. Barankov, K. Wei, B. Samson, and S. Ramachandran, "Resonant bend loss in leakage channel fibers," *Opt. Lett.*, vol. 37, no. 15, pp. 3147–3149, Aug. 2012.

[33] C. Jollivet, B. N. Samson, L. Leick, L. Shah, M. C. Richardson, and A. Schulzgen, "Comparative study of light propagation and single-mode operation in large-mode area fibers designed for 2-µm laser applications," *Opt. Eng.*, vol. 54, no. 1, p. 011006, Jan. 2015.

Shengli Fan received the B.S. degree in optical science and technology from the School of Science, Harbin Institute of Technology, Shandong, China, in 2014. He is currently working toward the Ph.D. degree in optics at the College of Optics and Photonics, University of Central Florida, Orlando, FL, USA. His research interests include optical imaging, microscopy, inverse problem, and signal processing.

Seth Smith-Dryden received the B.S. degree in physics from Ohio State University, Columbus, OH, USA, in 2015. He is currently working toward the Ph.D. degree in optics and photonics at the University of Central Florida, Orlando, FL, USA. His current research interests include subsurface imaging, microscopy, and imaging spectroscopy.

Jian Zhao received the B.S. degree in optics from the School of Physics and Engineering, Sun Yat-Sen University, Guangzhou, China, in 2012, and the M.S. degree in optics, in 2014, from the College of Optics and Photonics, University of Central Florida, Orlando, FL, USA, where he is currently working toward the Ph.D. degree in optics. He has 13 publications. His research interests include microstructured fiber optics, deep-learning applications in optics, and ultrafast optics.

Stefan Gausmann received the B.S. and M.S. degrees in physics from RWTH Aachen University, Aachen, Germany, in 2014 and 2016, respectively, and the second M.S. degree in optics and photonics, in 2017, from the University of Central Florida, Orlando, FL, USA, where he is currently working toward the Ph.D. degree in optics and photonics. His current research interests include fiber lasers and optical fiber characterization.

Axel Schülzgen received the Ph.D. degree in physics from Humboldt-University of Berlin, Berlin, Germany. Since 2009, he has been a Professor of optics and photonics with CREOL, The College of Optics and Photonics, University of Central Florida, Orlando, FL, USA. He is also an Adjunct Research Professor with the College of Optical Sciences, University of Arizona, Tucson, AZ, USA. He has published more than 120 papers in peer-reviewed journals and holds six patents. He is a Fellow of the Optical Society of America.

Guifang Li (F'13) received the Ph.D. degree in electrical engineering from the University of Wisconsin at Madison, Madison, WI, USA. He is currently a Professor of optics, electrical and computer engineering and physics with the University of Central Florida, Orlando, FL, USA. His research interests include optical communications and networking, RF photonics, all-optical signal processing, free-space optics, and optical imaging. He served as a Deputy Editor for *Optics Express* and an Associate Editor for *Optical Networks*, *Chinese Optics Letters* and the IEEE PHOTONICS TECHNOLOGY LETTERS. He currently serves as the Overseas Associate Editor-in-Chief of *Frontiers of Optoelectronics*, and Associate Editor for the OSA's *Optica* and the IEEE PHOTONICS JOURNAL. He is a Fellow of the SPIE, the Optical Society of America, and the National Academy of Inventors. He received the NSF CAREER award, the Office of Naval Research Young Investigator Award, the UCF Research Incentive Award in 2006, and the UCF Innovator Award in 2012.

Bahaa E. A. Saleh (M'73–F'91–LF'09) received the Ph.D. degree from Johns Hopkins University, Baltimore, MD, USA, in 1971. He held faculty and research positions with the University of Santa Catarina, Brazil, with Max Planck Institute, Germany, with the University of California-Berkeley, with Columbia University, with the University of Wisconsin-Madison, and with Boston University, where he was the Chair with the ECE Department (1994–2008). He has been a Dean with the College of Optics and Photonics, University of Central Florida, Orlando, FL, USA, since 2009. His publications include more than 285 journal papers and three books: *Photoelectron Statistics* (Springer, 1978), *Fundamentals of Photonics* (Wiley, 2007, with M. C. Teich), and *Introduction to Subsurface Imaging* (Cambridge Univ. Press, 2011). His research interests include coherence and statistical optics, nonlinear and quantum optics, and image science. He was an Editor-in-Chief of the *Journal of the Optical Society of America A* (1991–1997) and the Founding Editor of the *OSA Advances in Optics and Photonics* (2008–2013). He is Fellow of OSA, APS, SPIE, and the Guggenheim Foundation. He received the OSA Beller Award, the SPIE BACUS award, the Kuwait Prize, the OSA Distinguished Service Award, and the OSA Mees Medal.